Technical Physics, 2025, Vol. 70, No. 10

09

Compact VLS-grating spectrograph for 3−20 nm range

© S.S. Morozov,[1] M.Yu. Znamensky,[2] S.A. Garakhin,[1] M.V. Zorina,[1] D.G. Reunov,[1] B.A. Ulasevich,[1] N.I. Chkhalo[1]

[1] Institute of Physics of Microstructures, Russian Academy of Sciences,
603087 Nizhny Novgorod, Russia
[2] NPO „State Institute of Applied Optics",
420075 Kazan, Russia
e-mail: morozov_sv@ipmras.ru

Received May 28, 2025
Revised May 28, 2025
Accepted May 28, 2025

A compact spectrograph for soft X-ray range using a variable line spacing (VLS) first-order diffraction grating. The design includes a set of innovative solutions offering smaller spectrograph dimensions for higher mobility and increased aperture ratio. The main optical components are mounted on a single base to avoid spectrograph optics mismatch. A commercial GSENSE2020BSI 13.3 × 13.3 mm CMOS matrix with a$6.5\,\mu$m pixel size and high detective quantum efficiency in the soft X-ray range was used as a detector. The spectrograph optics contains a focusing mirror with a double-layer reflective Cr-C coating offering an increased spectrograph aperture ratio. First-order diffraction efficiency of the grating was measured and, together with the calculated dependence of resolution on wavelength, indicates a sufficiently high definition of spectral imaging of a source. X-ray optical configuration of the spectrograph, design X-ray optical properties, 3*D* image and photograph of the spectrograph are provided.

Keywords: spectrograph, VLS grating, Cr/C double-layer mirrors, soft X-ray radiation, extreme ultraviolet radiation.

DOI: 10.61011/TP.2025.10.62078.119-25

Introduction

A compact high-resolution spectrograph is used to fulfil a wide range of scientific tasks in the field of soft X-ray (SX) and extreme ultraviolet (EUV) spectrometry both in laboratories and at MegaScience facilities. The widest class of tasks fulfilled using such instruments is plasma diagnostics in terms of radiation spectrometry of plasma produced by laser-induced and electrical breakdown [1–5]. This class of instruments may be also used at synchrotrons for analysis of inelastic processes induced by the interaction between X-ray radiation and a substance [6]. In this case, for example, to explore the processes associated with phonon excitation, energy resolution shall be in the order of 0.01 eV, for scattering by magnons, interband transitions and plasmons — energy resolution shall be 0.1 eV, 1 eV and 10 eV, respectively. In the vicinity of 100 eV, the appropriate instrument's spectral resolution $\Delta\lambda/\lambda$ is within $10^{-4}-10^{-1}$. For plasma spectroscopy, where ion lines with various degrees of ionization or ion material shall be reliably identified, a resolution of 10^{-3} is sufficient [7–9].

Only diffraction grating instruments have such resolution in the long-wavelength SX an EUV ranges [10–12], however, classical configurations with a spherical Rowland grating [13] or a plane grating [14] don't provide a flat dispersion field and are good only as large monochromator spectrometers.

Spherical variable line spacing gratings, so-called VLS gratings, offer brand new opportunities. Components of this type are used in small instruments because focusing properties of concave VLS gratings allow reducing the number of optical components in a system while maintaining a sufficiently high resolution. The first studies addressing spectrographs of this type were published by T. Harada [15,16]. They used a spherical VLS grating with the central groove frequency $p_0 = 1200\,\mathrm{mm}^{-1}$ and curvature radius $R = 5649$ mm. More advanced spectrograph configuration versions using a VLS grating are described, for example, in [17,18]. To date, the most compact high-resolution spectrograph with removable VLS grating has been created by FIAN [19]. The authors have achieved a quasi-plane focal curve providing high resolution in the order of 10^3.

This study describes the optical configuration, specifications and design of the existing spectrograph developed by the Institute of Physics of Microstructures, Russian Academy of Sciences. This spectrograph has a number of distinguishing features compared with one of the most advanced representatives of this class of instruments [19]:

– single platform encompassing all X-ray optical components and small dimensions allowing integration into an instrument, for example, a reflectometer described in [14], for analysis of a radiation spectrum reflected from a sample;

– focusing inlet mirror offering a multifold increase in the collecting aperture of the spectrograph, whilst the radiation focusing condition at the spectrograph entrance slit is maintained in a wide range of distances to the source by varying the angle of radiation incidence on the mirror;

– for stand-alone operation, the spectrograph is mounted in a single vacuum chamber with a 100 mm bore flange for

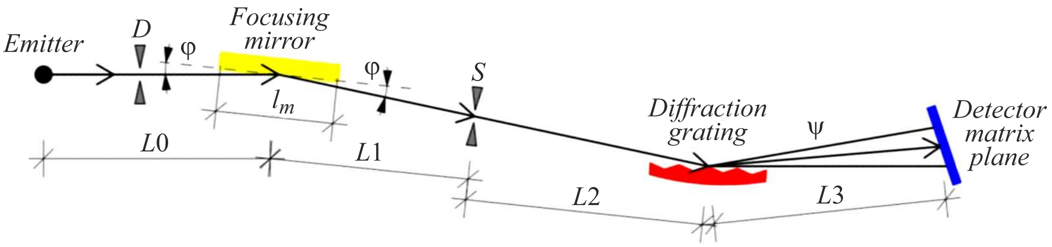

Figure 1. Optical configuration of the spectrograph: D — the diaphragm, φ — a sliding angle of radiation incidence on the mirror, l_m — a focusing mirror length, L0 — a distance between the radiation source and mirror, L1 — a mirror focusing distance, S — the slit, L2 — a the slit to diffraction grating, L3 — a distance from the grating to detector, ψ — a diffraction angle.

evacuation using a turbomolecular pump, which is critical for heavy gas ion measurements, where absorption in gas may have a dramatic effect on line intensity and spectrum shape as a whole [20].

1. Optical configuration and design specifications of the spectrograph

Schematic diagram of the spectrograph is shown in Figure 1. Optical configuration of the instrument consists of antiscatter diaphragm D designed to limit the dimensions of light flux transmitted further into the instrument; spherical focusing mirror FM that provides source imaging (or is set to any region on an extended source) on the entrance slit: instrument entrance slit S, whose monochromatic images are produced in the focal plane using the diffraction grating; spherical concave VLS diffraction grating that resolves the incident polychromatic radiation into spectral components, and matrix detector MD.

The instrument works in the following way. The focusing mirror collects light from the source on the slit. Because of using a total external reflection mirror with sliding geometry, the mirror reflects radiation with a short-wavelength boundary defined by the total external reflection angle [21], whilst, when the curvature radius is fixed in accordance with the spherical mirror focusing condition, the farther the source from the mirror the larger the sliding angle, and vice versa. Focusing provides considerable increase in the fraction of source radiation power used for spectrum readout, which has a positive effect on the measurement accuracy.

Then the diverging beam transmitted though the slit strikes the diffraction grating at a central angle of 6°. The angle in this case has been chosen according to the planned experiment conditions for investigation of emission characteristics of a laser plasma source being developed for a 11.2 nm lithography machine [22]. Owing to the optical properties of the grating, a spectral image of the source with a relatively high resolution may be produced on flat detector MD without relative movement of optical components during operation. Source imaging may be provided without using a VLS grating, but a properly selected variable line spacing has a positive effect on the flatness of the spectral focal curve and reduces aberration distortions, thus increasing the instrument resolution [18]. Requirement for maintaining a constant angle of incidence on the grating is an important feature of the VLS grating spectrograph, however, when distance to the source L0 is changed without changing the angle of focusing mirror FM, defocusing occurs on the slit. Thus, to maintain the optimum focus on the slit and the constant angle of incidence on the diffraction grating, the mirror is mounted on a four-axis mechanical table to provide adjustment of the angle of incidence to distance L0. It is necessary to ensure focusing on slit S for the X-ray reflected at a new angle, which is achieved by rotating the whole instrument about the focusing mirror axis. For this, the spectrograph is placed on a curved rail and connected to the test source through a bellows. The bellows and rail are not shown in Figure 1. Detector MD is tilted to provide the best conditions for viewing the spectral image of the source.

The VLS grating, despite the obvious benefits, also implies some difficulties. In particular, since the focusing conditions may be strictly adhered to only at a single wavelength, the focal curve may differ considerably from the straight line defining the detector plane.

It is known that the classical approach for VLS gratings is the expansion of groove frequency in a series of y:

$$p(y) = p_0 + p_1 y + p_2 y^2 + p_3 y^3, \tag{1}$$

where y is the distance perpendicular to the grating grooves, p_0 denotes the groove frequency in the center of the grating aperture, p_1 defines the spectral focal curve, p_2 and p_3 serve for compensation of the meridional coma aberration and spherical aberration, respectively [18].

Then the optical path function is introduced

$$F = l_1 + l_2 + m\lambda n(y), \tag{2}$$

where l_1, l_2 are the distances from the source to the center of grating and from the grating to the image, respectively, m is the diffraction order. Expanding F in a series of y and using the Fermi principle, the following relations may be derived for $p_0 \dots p_3$:

$$\cos\varphi - \cos\psi = m\lambda p_0, \tag{3}$$

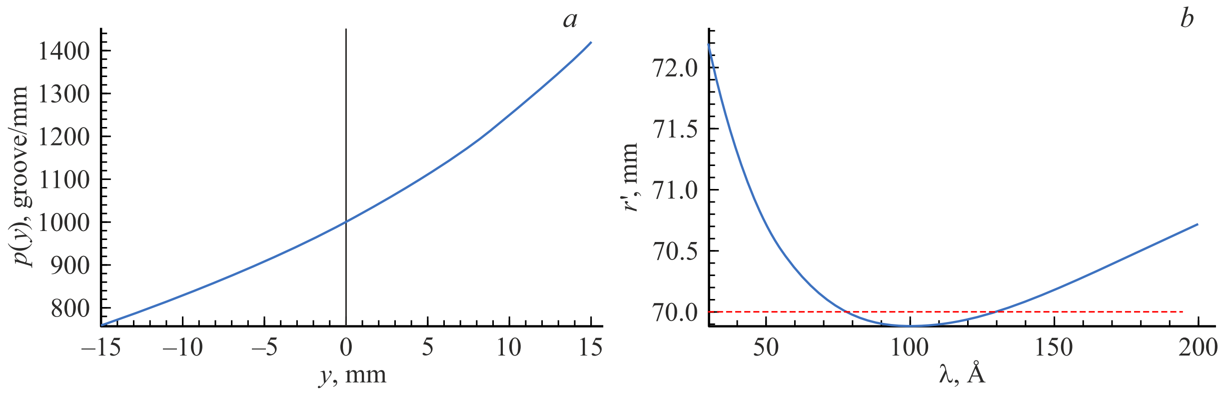

Figure 2. *a* — distribution of groove density along the grating, *b* — spectral focal curve. The focal distance of 70 mm is marked by a dashed line.

$$\frac{\sin^2\varphi}{r}-\frac{\sin\varphi}{R}+\frac{\sin^2\psi}{r'_h}-\frac{\sin\psi}{R}=m\lambda p_1, \qquad (4)$$

$$\frac{3}{2}\left[\frac{\cos\varphi}{r}\left(\frac{\sin^2\varphi}{r}-\frac{\sin\varphi}{R}\right)-\frac{\cos\psi}{r'}\left(\frac{\sin^2\psi}{r'}-\frac{\sin\psi}{R}\right)\right]=-m\lambda p_2, \qquad (5)$$

$$2\left[\left(\frac{\cos\varphi}{r}\right)^2\left(\frac{\sin^2\varphi}{r}-\frac{\sin\varphi}{R}\right)+\left(\frac{\cos\psi}{r'}\right)^2\times\left(\frac{\sin^2\psi}{r'}-\frac{\sin\psi}{R}\right)\right]-\frac{1}{2r}\left(\frac{\sin^2\varphi}{r}-\frac{\sin\varphi}{R}\right)^2-\frac{1}{2r'}\left(\frac{\sin^2\psi}{r'}-\frac{\sin\psi}{R}\right)^2=m\lambda p_3. \qquad (6)$$

In the given relations, r is the distance from the source to grating, r' is the distance to the focus, R is the grating curvature radius, ψ is the diffraction angle, φ is the sliding angle.

$p_1 \ldots p_3$ are calculated from relations (4)–(6) by defining the focusing condition for the specified wavelength λ at the specified distance r'. Grating curvature and distance to the diverging beam (slit) source were the optimization variables in our case.

Thus, by optimizing the grating parameters and distances between the entrance slit and detector, an optimum focus at a specified wavelength may be achieved. Then, since the spectral width of the slit (spectral slit image width) is directly related to the resolution as

$$R_c=\frac{\lambda}{S\,\frac{d\lambda}{dl}}, \qquad (7)$$

by calculating the spectral width of slit S (in our case — the spectral width of a point source) in the detector plane and linear dispersion $\frac{dl}{d\lambda}$, instrument resolution in the specified wavelength range may be inferred. Note that the dispersion and spectral width of slit also depend on the detector plane arrangement with respect to the focal curve. This parameter was optimized considering the approximation of the spectral width of the slit to the detector matrix pixel size ($6.5\,\mu$m) in as wide wavelength range as possible.

$\varphi = 6^\circ$, $r' = r = 70$ mm and $p_0 = 1000$ were initially chosen primarily for considerations of high diffraction grating efficiency in the operating wavelength range and compact size. Optimization to 3–20 nm provided the following grating variables: $R = 712.5$ mm, groove frequency corresponds to the following distribution (Figure 2, *a*, relation (8)):

$$p(y)=1000+20.2991\cdot y+0.3963\cdot y^2+0.0079\cdot y^3. \qquad (8)$$

Such groove distributions may be achieved, for example, through an optical holography process accomplished by GIPO (Kazan).

Figure 2, *b* shows the spectral focal curve. It can be seen that ideal focusing is achieved at two wavelengths — at 80 AA and 130 Å. At other wavelengths, „smearing“ of the spectral image of the point source is observed.

Relative arrangement of the detector plane and focal curve in a real optical configuration is shown in Figure 3.

In Figure 3, the center of the diffraction grating is in the origin of coordinates. The calculation implies that the total height of the point source image within 3–20 nm will be in the order of $S_0 = 6.7$ mm in the detector plane. This means that the source image size fits into the matrix size that is equal to 13.3 mm in height.

Knowing the dependence of the point source image width on the observed radiation wavelength, and having calculated the linear dispersion in the detector plane, the dependence of the instrument resolution on wavelength may be derived.

R_c related to the inverse linear dispersion and spectral width of slit S through (7) is the fullest spectral characteristic of spectrographs.

Note that the calculation of resolution using relation (7) considers only geometrical defocusing. Final detector pixel size equal to $6.5\,\mu$m is a considerable limitation of the maximum resolution in this case. Red curve on the diagram

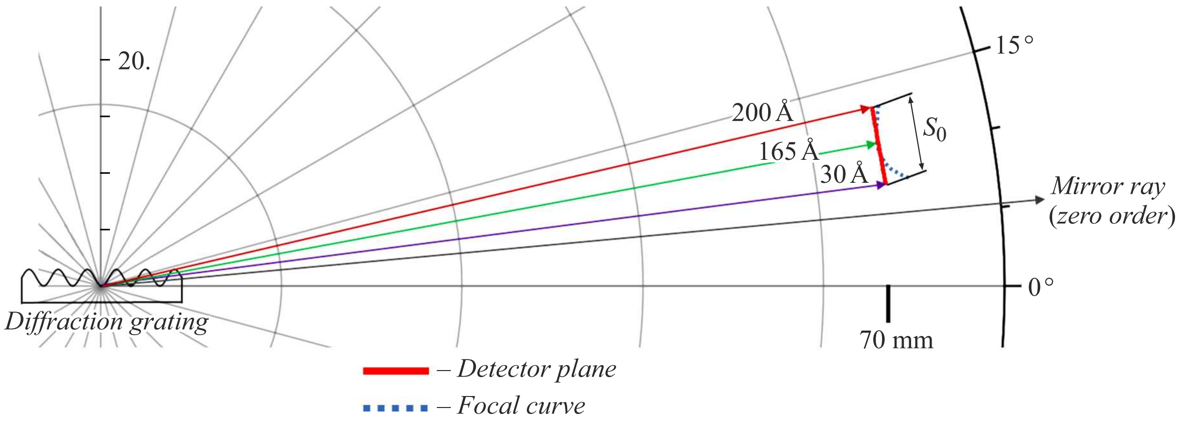

Figure 3. Comparison of the focal curve and detector spatial arrangement.

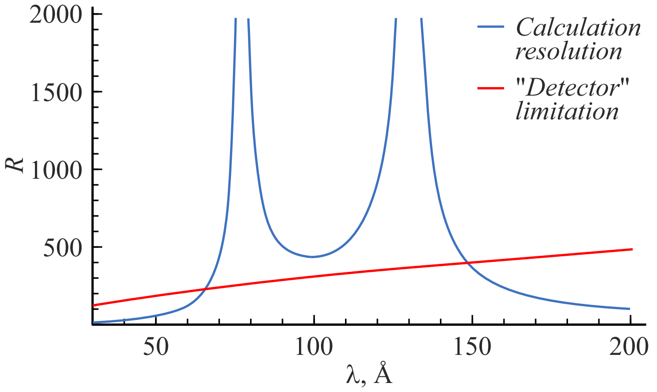

Figure 4. Blue curve corresponds to the resolution calculated considering geometrical defocusing. Red curve displays resolution limitation related to the detector pixel size.

$R(\lambda)$ shown below denotes this limitation. Red curve shall be considered to be of higher priority in the ranges where the blue curve lies above the red one. For a calculation of the aberration effect on the resolution of such spectral instrument, see, for example, [23].

Dependence of the resolution on wavelength is shown in Figure 4.

In accordance with the foregoing dependence of the resolution on radiation wavelength in the point source approximation, spectral resolution for radiation near $\lambda = 100$ Åwill be approximately equal to 0.16 Å when using a matrix with the..... pixel size. 6.5 μm.

$R(\lambda)$ throughout the wavelength range is not higher than 400.

2. Formation of the VLS grating and specifications of spectrograph components

Grating with the above-mentioned distribution was formed using a holographic technique by GIPO, Kazan. Grating recording geometry and main dimensions are shown in Figure 5, *a*. Grooves are formed by interference of two coherent spherical waves of point sources produced by focusing laser radiation on small apertures *A* and *B*. Laser wavelength is $\lambda = 441.6$ nm. The calculated groove frequency differs slightly from the target one (Figure 5, *b, c*) because of the specifics of the holographic grating recording process.

Diffraction efficiency of the grating was measured on the reflectometer based on the PCM-500 monochromator spectrometer using a classical scheme where radiation strikes the grating placed in the center of the test chamber at a particular sliding angle (here — 6°). Diffracted radiation is captured by the detector secured on the goniometer arm. The detector moves along the fixed radius at an angle around the grating, angle on the x axis (Figure 6) is the detector angle with respect to the probe beam. Thus, 12° in Figure 6 corresponds to the mirror order.

It follows from Figure 6 that the diffraction efficiency of the initial Al-coated grating in the operating sequence is from 4 % to about 12 % within 11.4–16 nm. Thus, efficiency, especially far from the center of the range ($\lambda < 6$ nm and 16–20 nm) is low, in particular due to considerable roughness that is approximately equal to 5–7 nm according to atomic force microscopy measurements. However, we hope to considerably increase the grating efficiency many-fold in future: first, by means of ion polishing that dramatically reduces groove roughness [24]; second, by deposition of high-reflection double-layer Cr/C coating, whose reflection coefficient is much higher in this range as that of aluminum used in the test grating.

The spectrograph configuration uses a spherically curved $30 \times 30 \times 10$ mm fused silica wafer with curvature radius $R = 712.5$ mm as a collecting mirror. Double-layer Cr/C coating with demonstrated superiority in this wavelength range compared with all other layers, including Au, was used as reflective coating as in the diffraction grating case [25].

To date, the mirror has been made. Actual curvature radius was 711.3 mm, which corresponds to the angle of

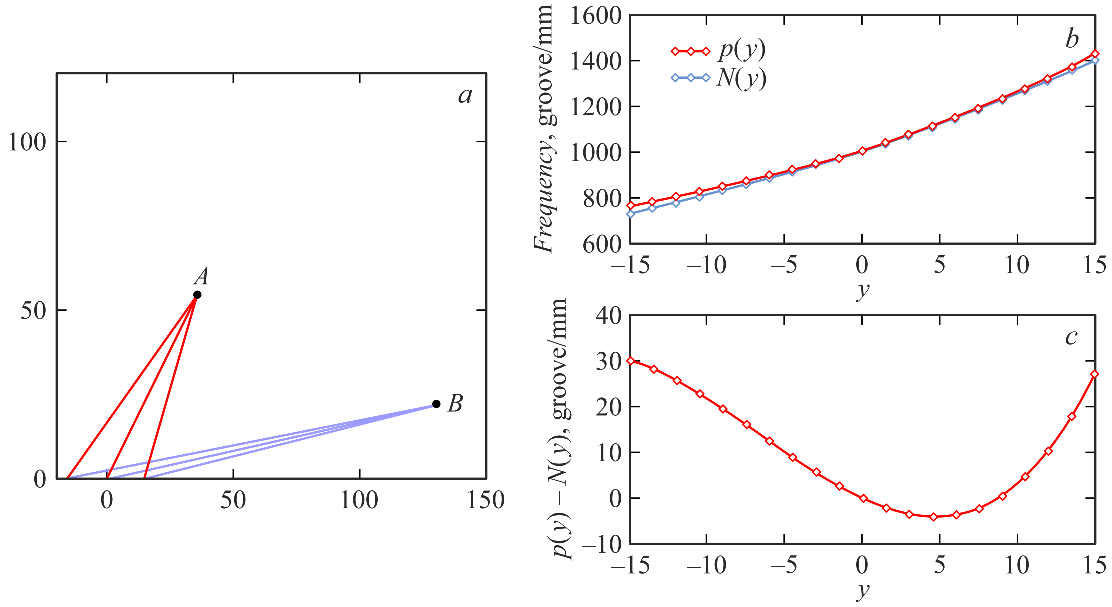

Figure 5. *a* — grating recording geometry (source arrangement), *b* — comparison between the target and nearest possible groove frequencies, *c* — difference between the target and nearest possible groove frequencies.

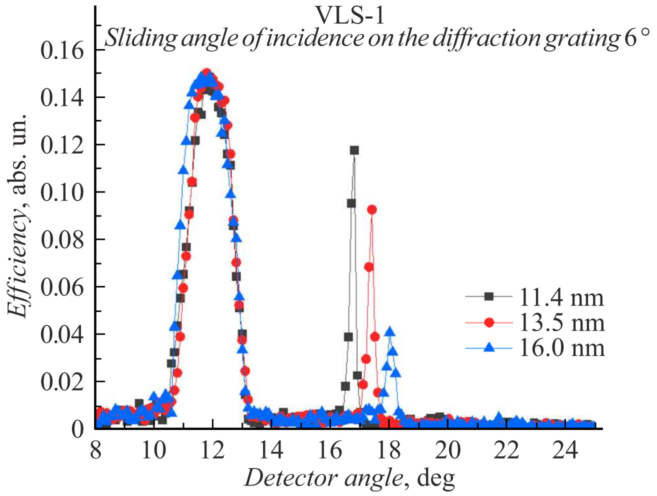

Figure 6. Diffraction efficiency of the VLS grating.

incidence of 10° with nominal distances of 500 mm between source and mirror and of 70 mm between the mirror and slit . Roughness within the spatial frequency range of $0.025{-}65\,\mu\text{m}^{-1}$ was about 1 nm, RMS depth of surface asphericity was 7 nm. These parameters are indicative of good quality of the wafer, which provides effective radiation focusing on the slit after deposition of the reflective coating.

GSENSE2020BSI 4 MP CMOS matrix with a $6.5\,\mu$m pixel size was used as the detector. Photosensitive zone dimensions are 13.3×13.3 mm (2048×2048 pixels), dynamic range is about 90 dB. Readout noise of this matrix is max.1.6 e^{-}. Maximum frame repetition rate is 74 frames per second. The detector has a high quantum efficiency ($\geq 80\,\%$) within 3–20 nm (data taken from the manufacturer web site [26]).

3. Spectrograph manufacturing

Design documentation was prepared in accordance with the drawing in Figure 1. Figure 7 shows a 3D model of spectrograph without a vacuum chamber wall (Figure 7, *a, b*) and top flange (Figure 7, *c*).

The mirror and grating are secured on the tables with four degrees of freedom allowing the optics to be tuned to a particular source. This spectrograph uses a CMOS matrix with combined cooling: Peltier cooling and Peltier rear-side water cooling. The matrix is mounted on the adjustable bellows assembly to provide adjustment of the distance between the matrix and diffraction grating as well as of the slope to the plane with respect to the zero beam, with an X-ray beam, thus, ensuring the maximum resolution. The chamber diameter is 400 mm, making this instrument sufficiently compact.

To date, all spectrograph assemblies have been prepared and the spectrograph has been assembled (Figure 8).

A series of experiments has been planned for spectral measurements of laser plasma sources used by the Institute of Physics of Microstructures, Russian Academy of Sciences, by means of the spectrograph.

Conclusion

The study describes a relatively compact high-numerical-aperture high-resolution spectrograph based on a VLS grating and matric detector. Optical component simulation

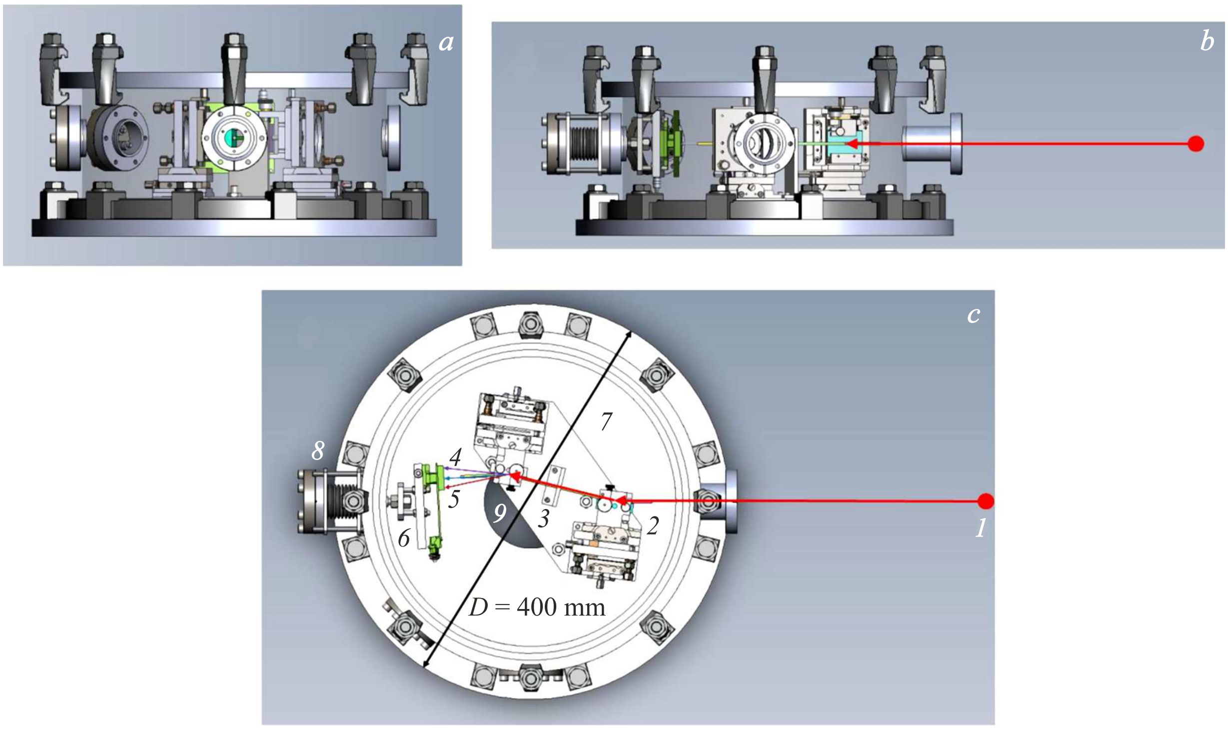

Figure 7. Spectrograph model assembly; *a* — view when looking from the source, *b* — side view, *c* — plan view: *1* — assumed source position, *2* — focusing mirror secured on the table with translation stages, *3* — slit, *4* — VLS grating secured on the table with translation stages, *5* — CMOS matrix on board, *6* — CMOS matrix cooling element, *7* — spectrograph chamber, *8* — bellows assembly for liquid cooling of the matrix, *9* — location of opening for evacuation, red arrow shows X-ray direction. The following components are not shown: bellows for joining the spectrograph to the test source, curved rail, on which the instrument is mounted, and turbomolecular pump placed in the instrument bottom.

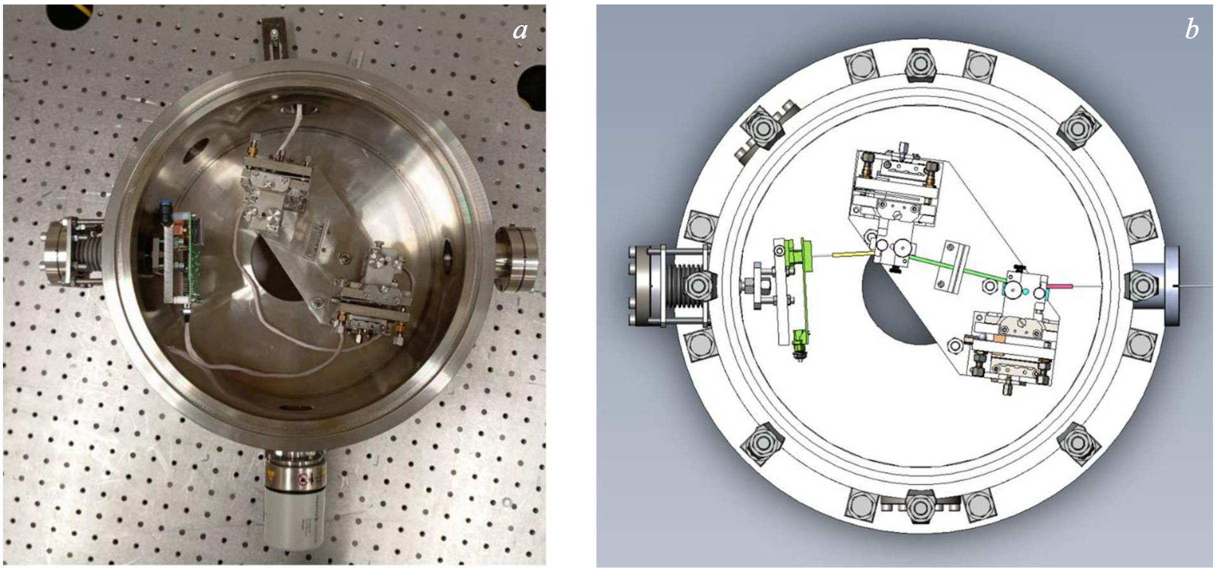

Figure 8. Left — photograph of the spectrograph assembly, right — plan view of the assembly model.

process, calculation of spectral characteristics and compact spectrograph configuration for a 3–20 nm range were described in detail. The calculated spectral characteristics of the spectrograph are a little lower than those of large stationary Rowland, Czerny-Turner and Harada grating spectrometers [13,14,18]. However, small dimensions, common spectrograph chambers encompassing all components, collecting focusing mirror and effective handling of sources at different distances from the spectrograph, stand-alone evacuation and *in situ* adjustment of detector's focal plane make this instrument much-needed for X-ray plasma and solid-body spectroscopy.

Funding

The study was performed under state assignment № FFUF-2024-0022 in terms of engineering design, and grant of the Russian Science Foundation № 21-72-20108-P in terms of manufacturing and tuning.

Conflict of interest

The authors declare no conflict of interest.

References

[1] H. Fiedorowicz, A. Bartnik, M. Szczurek, H. Daido, N. Sakaya, V. Kmetik, Y. Kato, M. Suzuki, M. Matsumura, J. Tajima, T. Nakayama, Th. Wilhein. Opt. Commun., **163** (1–3), 103 (1999). DOI: 10.1016/S0030-4018(99)00100-5

[2] F. Gilleron, M. Poirier, T. Blenski, M. Schmidt, T. Ceccotti. J. Appl. Phys., **94** (3), 2086 (2003). DOI: 10.1063/1.1587264

[3] A. Bartnik, P. Wachulak, T. Fok, Ł. Wegrzynski, H. Fiedorowicz, T. Pisarczyk, W. Skrzeczanowski, T. Chodukowski, Z. Kalinowska, R. Dudzak, J. Dostal, E. Krousky, J. Skala, J. Ullschmied, J. Hrebicek, T. Medrik. Plasma Phys. Control. Fusion, **58**, 014009 (2016)

[4] A. Bartnik, H. Fiedorowicz, R. Jarocki, J. Kostecki, M. Szczurek, P.W. Wachulak. Nuclear Instruments and Methods in Physics Research Section A: Accelerators, Spectrometers, Detectors and Associated Equipment, **647** (1), 125 (2011). DOI: 10.1016/j.nima.2011.05.033

[5] N.I. Chkhalo, S.A. Garakhin, A.Ya. Lopatin, A.N. Nechay, A.E. Pestov, V.N. Polkovnikov, N.N. Salashchenko, N.N. Tsybin, S.Yu. Zuev. AIP Advances, **8** (10), 105003 (2018). DOI: 10.1063/1.5048288

[6] A.I. Chumakov, A. Barla, R. Rüffer, J. Metge, H.F. Grünsteudel, H. Grünsteudel, J. Plessel, H. Winkelmann, M.M. Abd-Elmeguid. Phys. Rev. B, **58** (1), 254 (1998).

[7] T. Fujimoto, S.A. Kazantsev. Plasma Phys. Controlled Fusion, **39** (9), 1267 (1997).

[8] S. Alexiou, A. Calisti, P. Gauthier, L. Klein, E. Dalimier, R.W. Lee, R. Stamm, B. Talin. J. Quantitative Spectroscopy and Radiative Transfer, **58** (4–6), 399 (1997).

[9] V.A. Boiko, A.Ya. Faenov, S.A. Pikuz. J. Quantitative Spectroscopy and Radiative Transfer, **19** (1), 11 (1978).

[10] M. Boots, D. Muir, A. Moewes. J. Synchrotron Radiation, **20** (2), 272 (2013).

[11] D.L. Voronov, R. Cambie, R.M. Feshchenko, E.M. Gullikson, H.A. Padmore, A.V. Vinogradov, V.V. Yashchuk. Proc. SPIE 6705, Advances in X-Ray/EUV Optics and Components II, 67050E (20 September 2007). DOI: 10.1117/12.732658

[12] I. Sakelliou, J.R. Peterson, T. Tamura, F.B.S. Paerels, J.S. Kaastra, E. Belsole, H. Böhringer, G. Branduardi-Raymont, C. Ferrigno, J.W. den Herder, J. Kennea, R.F. Mushotzky, W.T. Vestrand, D.M. Worrall. Astronomy Astrophys., **391** (3), 903 (2002).

[13] S.A. Garakhin, E.S. Antyushin, M.A. Barysheva, A.E. Pestov, V.N. Polkovnikov, R.S. Pleshkov, R.M. Smertin, N.I. Chkhalo. ZhTF, (in Russian) **94** (8), 1250 (2024).

[14] S.A. Garakhin, I.G. Zabrodin, S.E. Zuev, I.A. Kas'kov, A.Ya. Lopatin, A.N. Nechay, V.N. Polkovnikov, N.N. Salashchenko, N.N. Tsybin, N.I. Chkhalo, M.V. Svechnikov. Quant. Electron., **47** (4), 385 (2017).

[15] T. Harada, M. Itou, T. Kita. *A Grazing Incidence Monochromator With A Varied-Space Plane Grating For Synchrotron Radiation*, Proc. SPIE 0503, Application, Theory, and Fabrication of Periodic Structures, DiffractionGratings, and Moire Phenomena II (12 December 1984). DOI: 10.1117/12.944821

[16] T. Kita, T. Harada, N. Nakano, H. Kuroda. Appl. Opt., **22**, 512 (1983).

[17] A.O. Kolesnikov, E.A. Vishnyakov, A.N. Shatokhin, E.N. Ragozin. Quant. Electron., **49** (11), 1054 (2019).

[18] E.A. Vishnyakov, A.O. Kolesnikov, E.N. Ragozin, A.N. Shatokhin. Kvantovaya elektronika, **46** (10), 953 (2016) (in Russian).

[19] M.V. Zorina, S.A. Garakhin, A.O. Kolesnikov, E.N. Ragozin, A.A. Solov'ev, A.N. Shatokhin. Bull. Lebedev Phys. Institute, **51** (4), S337 (2024). DOI: 10.3103/S1068335624601304

[20] J. Beckers, T. van de Ven, R. van der Horst, D. Astakhov, V. Banine. Appl. Sci., **9**, 2827 (2019). DOI: 10.3390/app9142827

[21] A.V. Vinogradov, I.A. Brytov, A.Ya. Grudsky, M.T. Kogan, I.V. Kozhevnikov, V.A. Slemzin. *Zerkalnaya rentgenovskaya optika* (Mashinostroenie, L., 1989) (in Russian)

[22] N.I. Chkhalo. Russ Microelectron, **53**, 397 (2024). DOI: 10.1134/S1063739724600511

[23] E.A. Vishnyakov, A.O. Kolesnikov, E.N. Ragozin, A.N. Shatokhin. Opt. Spectr., **125** (5), 783 (2018). DOI: 10.1134/S0030400X18110346

[24] S.A. Garakhin, M.V. Zorina, S.Yu. Zuev, M.S. Mikhaylenko, A.E. Pestov, V.N. Pleshkov, V.N. Polkovnikov, N.N. Salashchenko. Tech. Phys., **65**, 1780 (2020). https://doi.org/10.1134/S1063784220110110

[25] N.I. Chkhalo, P.K. Gaikovich, N.N. Salashchenko, P.A. Yunin, S.Yu. Zuev. Thin Solid Films, **598**, 156 (2016).

[26] Electronic source. Available at: https://www.gpixel.com/en/pro_details_1194.html

Translated by E.Ilinskaya